Article

Evaluating Frequency Domain Reflectometry as a Tool for Lithium-Ion Battery Health Prognosis

Ama Baduba Asiedu-Asante [1,*], Volker Pickert [1], Mohamed Mamlouk [1] and Charalampos Tsimenidis [2]

[1] School of Engineering, Newcastle University, Newcastle Upon Tyne NE1 7RU, UK; volker.pickert@ncl.ac.uk (V.P.); mohamed.mamlouk@newcastle.ac.uk (M.M.)

[2] Department of Engineering, School of Science and Technology, Nottingham Trent University, Nottingham NG1 4FQ, UK; charalampos.tsimenidis@ntu.ac.uk

[*] Correspondence: a.b.asiedu-asante2@newcastle.ac.uk

Abstract: Monitoring battery aging is crucial for maintaining reliability and performance. This study investigates Frequency Domain Reflectometry (FDR) as a tool for monitoring lithium-ion battery State-of-Health (SoH). While FDR has been applied in battery research, the existing literature fails to address SoH assessment and lacks studies on larger battery samples to provide more meaningful results. In this work, nineteen cells initially underwent Electrochemical Impedance Spectroscopy (EIS) to assess their degradation levels during cyclic aging. This work evaluates FDR's effectiveness in monitoring battery health indicators, such as capacity and equivalent series resistance (ESR), by correlating these with FDR-measured impedance between 300 kHz and 1 GHz. Analytical comparison between impedance measured before and after de-embedding processes were presented. The results show FDR reactance within 300 kHz–40 MHz correlates with EIS-measured ESR, suggesting its potential as a SoH indicator. However, reduced sensitivity and accuracy, particularly after de-embedding, may limit practical applicability. Additionally, resonance-based analysis was conducted to explore the relationship between changes in circuit resonance and cell dielectric permittivity. Despite having the lowest sensitivity, the method showed that the resonance frequencies of cells remain relatively constant, mirroring behaviours associated with changes in resistive properties. Overall, this study provides insights into FDR's potential for battery diagnostics while highlighting avenues for future research to enhance effectiveness in real-world scenarios.

Keywords: Frequency Domain Reflectometry; battery State-of-Health; lithium-ion batteries; electrochemical impedance spectroscopy

1. Introduction

Lithium-ion (Li-ion) batteries play a pivotal role in electric vehicles, consumer electronics, energy storage, and renewable energy systems. They offer higher energy density (23–70 Wh/kg), a lower self-discharge rate, relatively high cell voltage, and durability [1]. However, their use and exposure to environmental conditions can degrade performance. This adversely affects their ability to store energy, meet power requirements, and eventually shorten their lifespans. Thus, the detection and characterisation of cell degradation are crucial for improving the battery performance, lifespan, and reliability of the systems that employ them. The characterisation of cell degradation is also vital in determining a cell's suitability for second-life applications and can help shape the future of battery manufacturing.

Degradation of Li-ion cells is caused by the interaction between a myriad of physical and electrochemical processes. These processes are complex and occur across overlapping timescales, complicating their study. Capacity fade and an increase in internal impedance are known indicators of degradation [1–3]. The ohmic resistance encompasses the internal resistance of components such as electrodes and electrolytes, while the capacitance is related to the dielectric properties of the electrolyte. Various techniques, including Electrochemical Impedance Spectroscopy (EIS), have been used to measure these parameters. EIS

is a well-established impedance measurement method that has proven effective in studying degradation mechanisms and dynamic battery characteristics, such as mass transport processes [4], internal impedance measurement [1,2,5], and the formation of a Solid Electrolyte Interface (SEI) layer [2].

Reflectometry is another well-established technique for detecting and characterising impedance discontinuities. It operates by sending high-frequency electromagnetic waves of various frequencies through a system or material. Depending on the impedance of the systems or materials under test, part of incident signal is reflected, and part is transmitted through it. System impedance characterisation is performed by analysing the reflected and transmitted signals. There are several forms of reflectometry, each of which is distinguished by the type of the incident signal used. In previous studies [6–8], time-domain reflectometry (TDR), frequency-domain reflectometry (FDR), and spread-spectrum time-domain reflectometry (SSTDR) were effectively employed to detect and locate impedance irregularities in power lines (both overhead and subsea) and aircraft cables. FDR has also been used to measure the dielectric permittivity of soils and materials. In Masrakin et al. [9] and Skierucha and Wilczek [10], a resonator circuit based on FDR was designed such that its resonance frequency changed with the material being tested. By measuring the shift in the resonant frequency of the different dielectric materials, their respective capacitances and dielectric permittivity were determined.

Recent developments have extended reflectometry-based techniques to battery systems, notably in applications such as the assessment of batteries for power line communication (PLC) [11–13] and the evaluation of battery electromagnetic interference and compatibility (EMI/C) [14]. In such applications, the high-frequency characteristics of batteries in megahertz regions, which are typically outside the typical EIS range, are assessed. In Talie et al. [12] and Bolsinger et al. [13], while exploring the potential of using batteries as part of the communication channel in battery management systems (BMS), FDR was used to determine the high-frequency impedance of cells between 300 kHz and 30 MHz and 1–110 MHz, respectively. These studies characterised cells using equivalent models based (EEC) on high-frequency impedance measured using the reflection coefficient (S_{11}) method. However, the reflection method is less sensitive to impedance values of less than 1 Ω [15]. Therefore, this configuration is not ideal for detecting aging-associated impedance changes in batteries that tend to be small in magnitude. The more sensitive shunt-through method, outlined in Keysight Technologies [15] was used in Landinger et al. [16] to measure the transmission parameters S_{21} of Li-ion cells from 1 kHz to 300 MHz. Similarly, an EEC model that is based on the measured impedance was developed for cell characterisation. This was further used to compensate for the effects of mounts used in the setup. Based on the methods proposed in Landinger et al. [16], the authors in Hackl et al. [17] developed a generalised de-embedding method for use with a shunt-through setup when measuring the S_{21} parameters of the batteries. This method addresses the inconsistencies that arise when cells are mounted on specialised PCB connectors for connection to Vector Network Analysers (VNA). The PCB connectors consist of a battery holder mounted on a PCB board with two subminiature version-A (SMA) connectors for connection to VNAs [16]. In this method, the effects of the PCB connectors were removed by applying open, short, and load (OSL) impedance compensation to the measured data. The initial measured impedance obtained from the VNA that is calibrated using standard short, open, load, and through (SOLT) included influences from external mutual inductance between cells and the connectors, which was also compensated for by OSL compensation. In a study of the electrophysical processes of a cell at high frequency, Landinger et al. [11,18] employed this method to de-embed cell impedance from the measurement setup. An EEC model based on de-embedded impedance was developed, through which processes such as skin effects, ionic shunts, and resistive–inductive effects were identified. Furthermore, this study highlighted the dependency of high-frequency impedance on temperature, cell geometry, and design factors, such as winding and tab positions. The State-of-Charge (SoC) showed minimal influence on the measured impedance at frequencies up to 1 MHz.

These studies have applied high frequencies to measure battery impedance and have advanced knowledge by improving measurement setups, de-embedding protocols, modelling, and exploring impedance dependencies on temperature, SoC, and cell design. However, these tests have been carried out on either a single cell or a few cells, which raises the question of the universality of the method. Furthermore, these studies do not explicitly investigate the application of high-frequency impedance measurements for battery State-of-Health (SoH) estimation, nor do they evaluate the impact of SoH on the measured high-frequency impedance. It is noteworthy that the application of impedance measure to assess battery health has been studied in the literature, but these studies have been limited to lower frequency ranges and typically employed the EIS method [5]. Battery aging can cause various physical changes in the battery, which can influence the measured impedance, particularly at high frequencies. In Roy and Khan [19], the SSTDR method was applied to locate the degraded cells within a cell string. By establishing an initial reference when all cells in the string are healthy, aged cells are detected by the deviation of the subsequent measurement from the initial reference using sine-modulated pseudo-noise (SMPN) signals centered around 48 MHz. The effectiveness of this method in detecting the specific location of degraded cells in a series-connected lithium-ion battery pack shows deviations in measured high-frequency impedance from aging. However, the impact of battery strings on cells at various aging levels was not explored.

Therefore, this study investigates the use of FDR to monitor cell SoH by identifying the correlation between cell health indicators such as capacity and internal resistance and FDR impedance. This study differs in terms of the approach to utilising measured impedance. While previous studies solely focus the on measurement of impedance this study seeks to correlate the measured impedance with health indicators such as capacity and EIS-measured ESR to monitor battery SoH. This method has the potential to improve cell SoH characterisation by harnessing the ability of FDR to measure impedance and dielectric permittivity over a wide frequency range. The objective of this study is two-fold: First, to measure the high-frequency (HF) impedance of 19 cells exhibiting different levels of aging between 300 kHz and 1 GHz. This is accomplished using a setup based on both the S_{21} and ring resonator methods. Second, the aim was to apply the OSL compensation method proposed in the literature to de-embedding the cell impedance from the setup and perform a comparative analysis between results obtained before and after the de-embedding process was applied to the measured data. Additionally, a resonance-based method used in ring resonators was explored to investigate the relation between changes in cell resonance and cell dielectric permittivity. Cell capacity and internal resistance were obtained from cyclic aging and intermittent EIS testing.

The remainder of this paper is organised as follows. Section 2 presents the research methodology, the cell aging processes, and test setups for the EIS and FDR tests. In addition, de-embedding and the definition of the region of confidence are described in this section. Section 3 discusses the results and presents a comparative analysis of the resonance method with the responses obtained before and after the de-embedding process applied to the measured data. Finally, Section 4 presents the conclusions.

2. Materials and Methods

The samples used are 19 commercial LIR2032 coin cells rated 4.2 V, 40 mAh. The cells were composed of a lithium cobalt oxide ($LiCoO_2$) cathode and a graphite (C) anode coated on aluminum and copper current collectors, respectively [20]. The cell separator was made of polyethylene (PE), which was soaked in an electrolyte composed of a blend of ethylene carbonate ($C_3H_4O_3$) and lithium hexafluorophosphate ($LiPF_6$) [20]. With the separator placed between the coated cathode and the anode current collector foils, all three were rolled into a flat jelly roll, as shown in Figure 1. The anode and cathode tabs were placed at opposite ends of the jelly fold. Figure 1a, adapted from Woehrle [21], illustrates the flat jelly roll arrangement of the electrodes and separator in the cell, and Figure 1b shows an

image of the internal structure of the LIR2032 cell, highlighting the tap positions. Figure 1b was obtained by opening the cell in a Braun UNILAB glovebox.
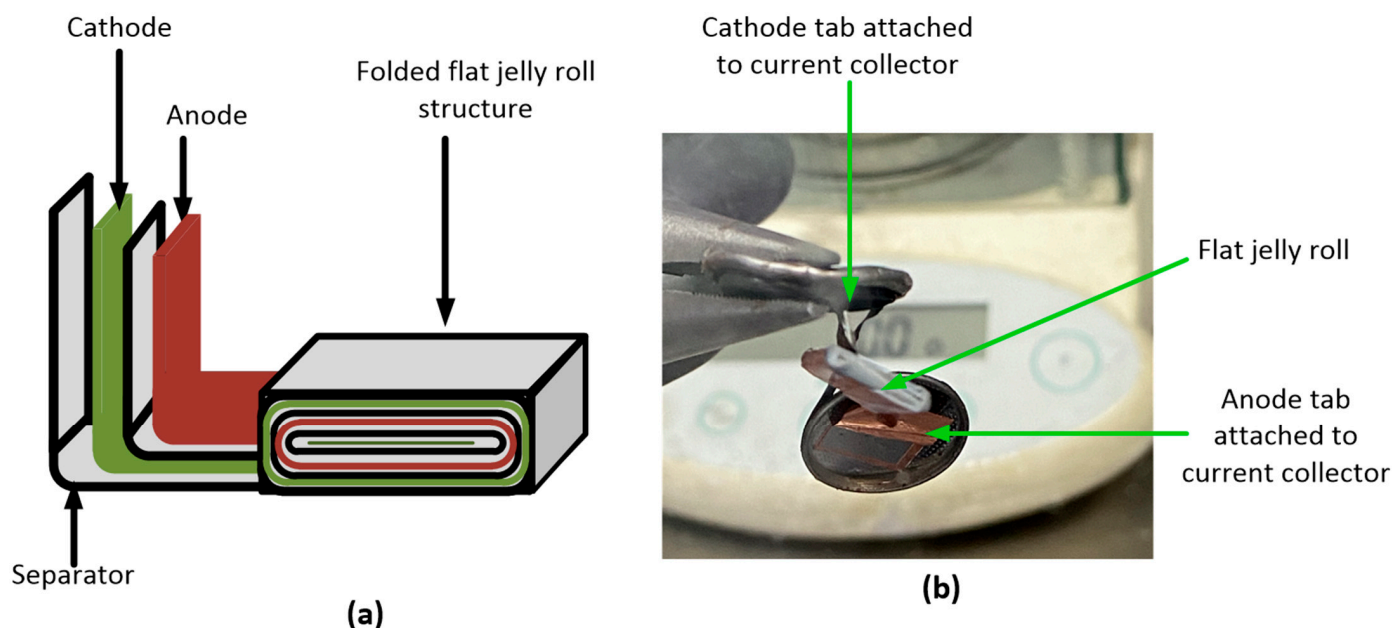

Figure 1. Cell structure (**a**) arrangement of cell electrodes and separator into flat jelly roll [21]. (**b**) Image of internal arrangement of cell taken.

Three experiments were performed concurrently on these cells: cell cycling, EIS, and FDR tests. The cells were aged through cycling, and EIS tests were performed to monitor impedance changes in the cells during aging and to characterise the degradation of the cells. The responses from the cycling and EIS tests provided the health indicators used to evaluate the performance of the FDR method. EIS and FDR tests were conducted intermittently after every 20th cycle during the cyclic aging process.

2.1. Cell Cycling

The constant current–constant voltage (CC–CV) method was used in cycling. This was performed at 25 °C with an end charge voltage of 4.2 V and a discharge cut-off voltage of 2.75 V. Initially, all cells underwent two cycles at a rate of 0.05C. This slow cycling ensured the initial formation of an SEI layer [22]. This also ensured that the aging effects observed during the subsequent cycling tests were not due to factors related to inconsistent electrode–electrolyte interfaces among the samples. After the initial slow cycles, the samples were divided into two batches. The first batch, herein referred to as Batch A, underwent the next 60 cycles at a rate of 1C, while the remaining cycles were performed at a 2C rate. Concurrently, cells within the alternate cohort, designated as Batch B, were cycled at a rate of 2C after the initial two slow cycles. This was performed to introduce variability into the samples under investigation.

Furthermore, cells 18 and 19 of Batch A were exposed to high discharge currents during cycles 14–22 and 270–300, respectively. Cycling was performed using a Maccor 4200 cycler, with the cells placed in a Binder FD 115 environment chamber for temperature control. Overall, 19 samples were aged for 102–442 cycles. The numbers of sample cycles and capacities are listed in Table 1.

Table 1. Aging indicators for sample cells.

Cell ID	Number of Cycles	Capacity (%)	EIS-Based ESR at Aged State (Ω)		Charge Transfer Resistance (Ω)		Double Layer Capacitance (F)		Resistance of SEI Layer (Ω)	
			Value in Ω	Percentage Increase (%)	New State	Aged State	New State	Aged State	New State	Aged State
Cell 1	102	45	0.204	7.0	0.735	1.434	0.024	0.055	1.209	1.241
Cell 2	102	62	0.217	5.8	0.396	1.397	0.085	0.104	1.980	1.398
Cell 3	102	50	0.220	1.9	0.557	0.740	0.013	0.101	1.960	1.236
Cell 4	102	45	0.223	3.7	0.584	0.857	0.023	0.052	1.373	1.158
Cell 5	102	50	0.224	1.9	0.790	0.621	0.015	0.051	1.575	1.259
Cell 6	202	49	0.228	34.4	0.391	6.650	0.063	0.100	1.214	1.310
Cell 7	102	32	0.230	6.0	0.879	0.776	0.016	0.096	1.222	1.168
Cell 8	202	7	0.240	15.7	0.532	2.284	0.019	0.062	1.089	1.355
Cell 9	202	26	0.241	20.5	0.532	2.284	0.019	0.062	1.089	1.355
Cell 10	102	42	0.242	5.4	0.496	0.776	0.051	0.096	1.828	1.168
Cell 11	102	31	0.244	1.0	0.674	0.729	0.024	0.046	1.135	1.155
Cell 12	342	63	0.252	28.5	0.622	1.884	0.008	0.064	1.118	1.342
Cell 13	342	12	0.266	28.6	0.540	3.258	0.011	0.065	1.116	1.268
Cell 14	342	8	0.272	45.8	0.389	5.388	0.016	0.056	0.804	1.087
Cell 15	342	4	0.272	33.3	0.562	6.454	0.010	0.057	1.158	1.426
Cell 16	442	18	0.487	146.7	0.336	0.791	0.017	0.121	0.759	1.992
Cell 17	442	12	0.521	132.4	0.451	2.148	0.012	0.158	0.699	4.565
Cell 18	202	2	0.576	175.6	0.093	30.299	0.001	0.108	1.099	2.342
Cell 19	362	7	1.028	384.7	0.400	3.861	0.012	0.114	0.626	2.059

2.2. EIS Tests

EIS tests were performed on cells at 4.2 V, between 10 MHz and 100 kHz, with a test signal amplitude of 10 mV. An Autolab 302 N potentiostat was used for testing. All cells underwent a potentiostatic hold prior to testing. During the potentiostatic hold, the cells were held at 4.2 V until the current was below the rate of 0.01C (0.4 mA) to ensure that the cell voltage was stabilised before testing [22]. To characterise cell aging, the impedance response from EIS tests was fitted to an equivalent circuit model (ECM) using the custom built EISyfit software, 2021 version used in Perry and Mamlouk [4]. The parameters of the model were determined via local search and genetic algorithms. From the models, electrochemical processes such as charge transfer resistance, double layer capacitance, and resistance associated with SEI growth, which are known factors of aging, were identified and quantified. In addition, the equivalent series resistance (ESR), which represents the total internal resistance of the battery, was extracted from the impedance response.

2.3. FDR Measurement Setup

The VNA was employed in FDR impedance measurement [11,15,16]. Specifically, the VNA two-port shunt-through method was used to measure the S-parameters of the cells, which were then converted into impedance. Although all four S-parameters were measured, only the transmission coefficient (S_{21}) was considered in this study. This offers more sensitivity in low ohmic measurements compared to other S-parameters [13,15]. The S_{21} method is also equivalent to the four-terminal Kelvin-sensing method used in tests to eliminate the effects of test leads and unwanted resistance [15]. Shown in Figure 2a is the VNA measurement circuit for S_{21} measurement. V_s is the VNA signal source whose current

is limited by the series-connected 50 Ω resistor. Part of the source current is measured using the parallel-connected voltage sensor V_{in} and a 50 Ω resistor. This is compared with the transmitted signal for magnitude and phase calculations. As the current propagates through the circuit, a voltage drop occurs across the cell. This voltage drop is picked up by the port 2 voltage sensor V_T, which represents the measured S-parameters of both the cell and the connector PCB.
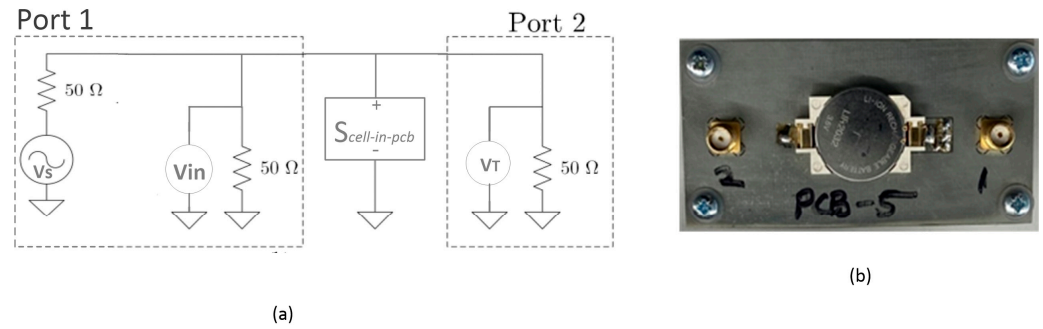

(a)

(b)

Figure 2. S-parameter measurement setup. (**a**) Circuit diagram for S-parameter measurement. (**b**) Image of measurement PCB.

The connector PCB was used to connect the cells to the VNA, shown in Figure 2b. The design uses two SMA connectors and a coin cell holder mounted on the PCB. These are connected such that the positive terminal of the cell holder connects to the inner pin of the SMA via the bottom plane of the PCB and the negative terminal connects the outer pins of the SMA through the top plane of the PCB. In addition to being suitable for S_{21} measurements, this PCB design was also based on the resonator design used in Masrakin [9]. The Pico106 VNA was used for FDR measurement. Prior to testing the cells, the VNA was calibrated using the short, open, load, and through (SOLT) calibration method. This was performed for a frequency range of 300 kHz to 1 GHz, with a source voltage of 0 dBm. The source voltage was chosen to attain a balance between measurement accuracy and cell linearity during the test. At 0 dBm, the dynamic range of the VNA was 90 dB, which ensured that the VNA could measure a wider range of signal levels. Thus, it can detect signals ranging from the VNA average noise floor level of −118 dB to signals of 90 dB or higher. As performed during the EIS test, the cells were placed in a prior potentiostatic hold before FDR tests.

The measured S_{21} parameter is defined as the ratio between V_{in} and V_T, as expressed in Equation (1) [23]. From this, the impedance was determined using Equation (2) [24]. In Equation (1), $V_{transmitted}$ refers to the transmitted voltage measured at port 2, and $V_{incident}$ refers to the incident voltage coming from port 1. Both voltages are complex values whose amplitude and phase shifts (in degrees) are measured by the VNA. Z_L is the complex impedance calculated from the S-parameters which, in this study, is the total impedance of the cell and PCB. Z_o is the system characteristic impedance established by the VNA manufacturer. The typical value of Z_o is 50 Ω [13,18].

$$S_{21} = \frac{V_{transmitted}}{V_{incident}} \tag{1}$$

$$Z_L = 25\frac{S_{21}}{1 - S_{21}} \tag{2}$$

De-Embedding and Region of Confidence Definition

The SOLT calibration compensated for the effects of the VNA impedance and test leads during the measurement. This implies that the measurement reference point is at the end of the leads; therefore, the impedance calculated from Equation (2) is the impedance of the cell plus that of the connector PCB, herein referred to as $Z_{cell-in-pcb}$. To obtain the cell impedance

only, Z_{cell}, the de-embedding method suggested in Hackl [17] was adopted. In this method, a matched load of 50 Ω is connected in place of the cell, and its S-parameters (S_{load}) are measured using the SOLT-calibrated VNA. Similarly, the S-parameters of a copper coin (S_{cu}) were measured. The copper coin was fabricated to have the same dimensions as the LIR2032 cell such that it possessed a similar range of external inductance values. The PCB was then measured with the cell holder terminals open and short-circuited to obtain S_{open} and S_{short}, respectively. Equation (2) was applied to S_{load}, S_{cu}, S_{open}, and S_{short} to obtain Z_{load}, Z_{cu}, Z_{open}, and Z_{short}, respectively.

Equation (3) was applied to shift the measurement reference point to the positive terminal of the cell holder [17]. This was performed for the cells and copper coin to obtain $Z_{cell\text{-}ext}$ and $Z_{cu\text{-}ext}$, respectively. Z_{sL} is the ideal value of the match load, that is, 50 Ω. Z_{inpcb} is replaced by $Z_{cell\text{-}in\text{-}pcb}$ to obtain $Z_{cell\text{-}ext}$, which includes the impedance of the cell and external inductive coupling effects between the cell and PCB planes. A similar procedure was performed using Z_{cu} to obtain $Z_{cu\text{-}ext}$. Using Equation (4), the effect of the external coupling between the cell and PCB planes is removed.

$$Z_{ext} = Z_{sL} \frac{\left(Z_{open} - Z_{Load}\right)\left(Z_{inpcb} - Z_{short}\right)}{\left(Z_{Load} - Z_{short}\right)\left(Z_{open} - Z_{inpcb}\right)} \tag{3}$$

$$Z_{cell-ext} = Z_{cell} + Z_{cu-ext} \tag{4}$$

In Hackl et al. [17], a region of confidence (RoC) was defined as the region within the spectrum where the open-circuit (Z_{open}) and short-circuit (Z_{short}) responses were the highest and lowest impedance values, respectively, and the load response (Z_{load}) was relatively closer to the open circuit than the short circuit. In this region, a cell with a relatively low impedance is expected to be closer to the short-circuit response. In this study, we added to this definition by identifying sections of the spectrum where changes in passive element responses were related to the changes in values of the respective element being measured. The RoC was defined for both the pre- and post-compensation stages using different values of resistors (R), inductors (L), and capacitors (C). Because this work involves the detection of changing values, this method of RoC definition helps to identify how the method detects changing values of resistive, inductive, and capacitive properties. This was performed for each analysis stage to identify the RoCs for each method and assess the overall setup sensitivity. For ease of reference, FDR impedance measured before the de-embedding process is herein referred to as pre-compensation, and impedance after the de-embedding is referred to as post-compensation.

First, the resonance-based method is used on the RLC responses obtained before de-embedding. Before de-embedding, resonance resulted from interactions between the PCB and inserted components, similar to those obtained in Masrakin et al. [9]. The resonance frequency shifted with the changing values of the elements. Hence, the variations in the resonance frequency can be related to the type and value of the element under test, as illustrated in Figure 3. The resonance frequencies of the inductors and capacitors decreased as their respective values increased. This was observed between 2 MHz and 130 MHz for inductors and between 4 MHz and 355 MHz for capacitors, as illustrated in green traces in Figure 3b and Figure 3c, respectively. This aligns with the inverse relationship between the resonance frequencies and the square root of the inductance and capacitance values. In contrast, the resonance frequency of the resistors, seen in Figure 3a (green trace), remained relatively stable between 123 MHz and 130 MHz. The absence of resonance in the 100 Ω resistor within the test frequency region can be attributed to its high impedance, which makes it behave like an open or overdamped circuit at the frequencies of interest. The changes observed in the resonance frequency of capacitors are particularly promising because cells behave like capacitors in their basic form. However, the sensitivity decreases with increasing capacitance. In the nano-Farads range, a 25 nF change in capacitance between 22 nF and 47 nF produced a 2 MHz change in resonance frequency, which was

further reduced to 1 a MHz change in resonance frequency from 57 nF to 100 nF. This suggests that, for coin cells with typical capacitance ranges between µF and mF, as seen in Table 1, this method might not be sensitive enough to detect changes in such value ranges.
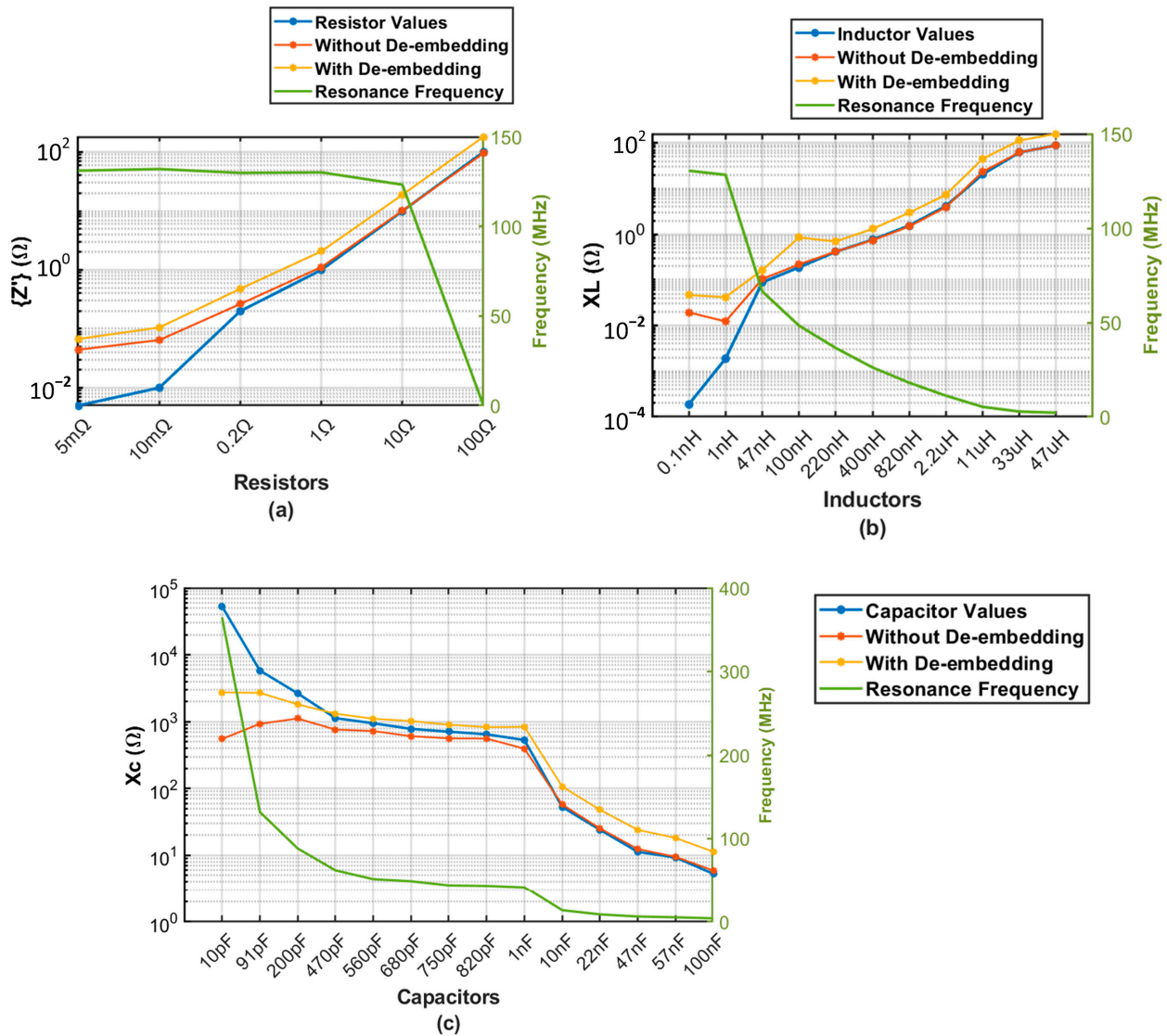

Figure 3. RLC resonance frequencies and impedance values from pre-compensation and post-compensation responses within the region of confidence. (**a**) Resistor responses, (**b**) inductor responses, (**c**) capacitor responses.

Outside the resonance region, changes in RLC responses that relate to variations in element values were observed between 300 kHz and 40 MHz. This behaviour was observed in both the pre-compensation and post-compensation responses. Within this region, the most accurate values are recorded at 300 kHz and are summarised in Figure 3a–c. A comparison between values obtained from pre-compensation and post-compensation responses and the calculated values at 300 kHz for each element are presented in Figure 3a–c. Overall, the recorded post-compensation impedances showed higher deviations than the recorded pre-compensation impedances for all RLC elements. This is because the de-embedding process compensates for PCB effects relative to cases of open, short, and load values, which can lead to deviations, especially when measuring very low impedances. Moreover, the measurements of low element values at both the pre- and post-compensation stages resulted in higher errors, indicating that achieving accuracy in the ranges of 5–10 mΩ, 0.1–1 nH, and 10–200 pF might be difficult for the setup. This limitation could hinder the

accuracy of the method in measuring some health indicators, particularly when small changes in quantity are involved. The RoCs were therefore defined to be between 300 kHz and 40 MHz for both pre- and post-compensation responses and between 2 MHz and 355 MHz for resonance-based analysis. Within these regions, there was improved sensitivity to variations in resistive, inductive, and capacitive changes but with limited accuracy. It is also noteworthy that the observed reduction in accuracy with the lowest values of elements and limited sensitivity at higher capacitance values may limit FDR performance when applied to the cells' more complex system, even within the RoC.

3. Results and Discussion

3.1. Sample Characterisation

The capacities of the 19 sample cells over their cycling durations are shown in Figure 4. Initially, cells 16, 17, and 19 from Batch A showed a relatively higher capacity for the first 60 cycles than those in Batch B, as shown in the Figure 4a insert. This is the result of slow cycling that allows cells to operate at close to optimal conditions, thereby reducing the stress on electrodes and the rate at which degradation mechanisms occur. As the C-rate is increased, so does the occurrence of electrochemical processes which facilitate further reduction in capacity after the first 60 cycles. This effect was also seen in the majority of cells from Batch B when the C-rate was increased from rates of 0.05C to 2C before and after cycle 2, respectively. Cells 18 and 19 showed a 23% and 28% decrease in capacity, respectively, after undergoing cycles with a high discharge current, as illustrated in Figure 4b. Again, additional electrochemical processes appeared to have been triggered, which caused a more rapid capacity loss during subsequent cycles.

Figure 5a shows a generic EIS impedance response of a commercial battery [25]. It summarises the literature on electrochemical processes associated with various time constants within the EIS impedance response and shows their respective frequency ranges and representations in a second-order ECM. Figure 5b shows the EIS impedance responses of the cells after their respective last cycles. It is observed that most cells in their aged state exhibit an enlarged second semicircle, leading to an increase in the impedance between the R_a and R_c points (in Figure 5a). This range is typically attributed to phenomena such as electrolyte decomposition and the formation and growth of the SEI layer. At the electrode–electrolyte interface, the decomposition of the electrolyte consumes the electrolyte components, reducing the ionic conductivity and capacity. Simultaneously, the SEI layer stabilises but grows with cycling, impeding lithium-ion transport and increasing internal resistance. This growth, if unstable, can also foster dendrite formation, further diminishing capacity. These processes collectively lead to an increased resistance to ion transport and charge transfer within the battery, which is exacerbated by the accumulation of lithium salts and other reaction by-products. In the aged state, cell 18 exhibits a significantly larger second semicircle and is devoid of the 45° diffusion process line. In this case, the effect of electrolyte decomposition and growth of the SEI layer is more pronounced, which impedes the diffusion of lithium ions, such that the diffusion rate is slowed to a timescale that falls out of the test frequency range. This can be attributed to the combination of the initial high discharge stress and prolonged cycling.

Another health indicator is the cell ESR. It is the high-frequency intercept point (Ra) in Figure 5a and represents the bulk resistance of the electrolyte solution and the resistance associated with the migration of ions through the electrolyte [14–16]. It has been employed as an aging indicator owing to its sensitivity to changes in the electrolyte composition and internal cell resistance. Therefore, similar to Figure 4a, the ESR values were extracted from the EIS impedance responses over cycling, as shown in Figure 6. Initially, the ESR value ranges from 0.17 to 0.24 Ω in the in the first few cycles. At their aged states, the resistances of cells in Batch B (cells 1–15) showed a slight and gradual increase to a range between 0.22 and 0.27 Ω. This gradual increase over cycling suggests that the ionic conduction resistance at the electrode–electrolyte interface and within the electrolyte increased with cycling. In Batch A, an increase of over 80% in ESR is observed for the cells. In cells 18 and 19, this

increase was observed after 22 and 300 cycles, respectively. This suggests that the ESR increment was worsened by the exposure of cells to high discharge currents during cycles 14–22 and 270–300, respectively. For cells 16 and 17, the increase was gradual, suggesting a cumulative effect of repeated cycling, change in C-rates, and stress on the electrodes and electrolyte as the cells reached approximately 442 of the intended 500 life cycles.
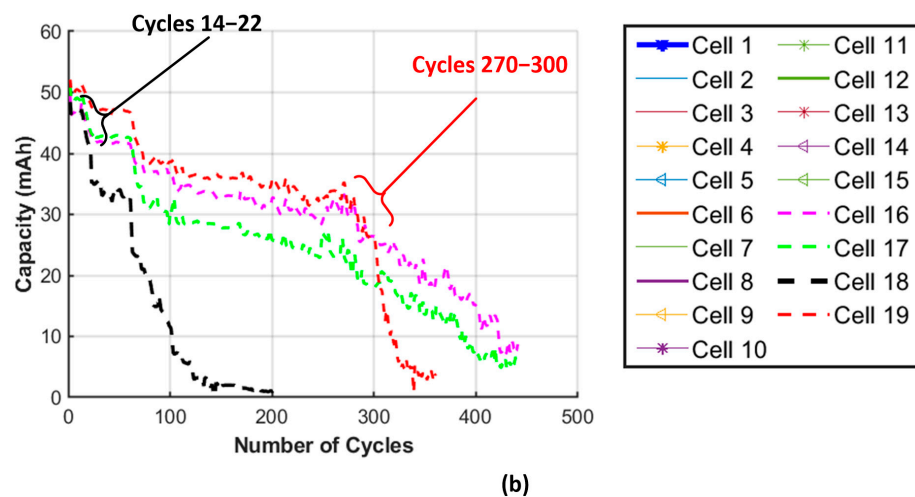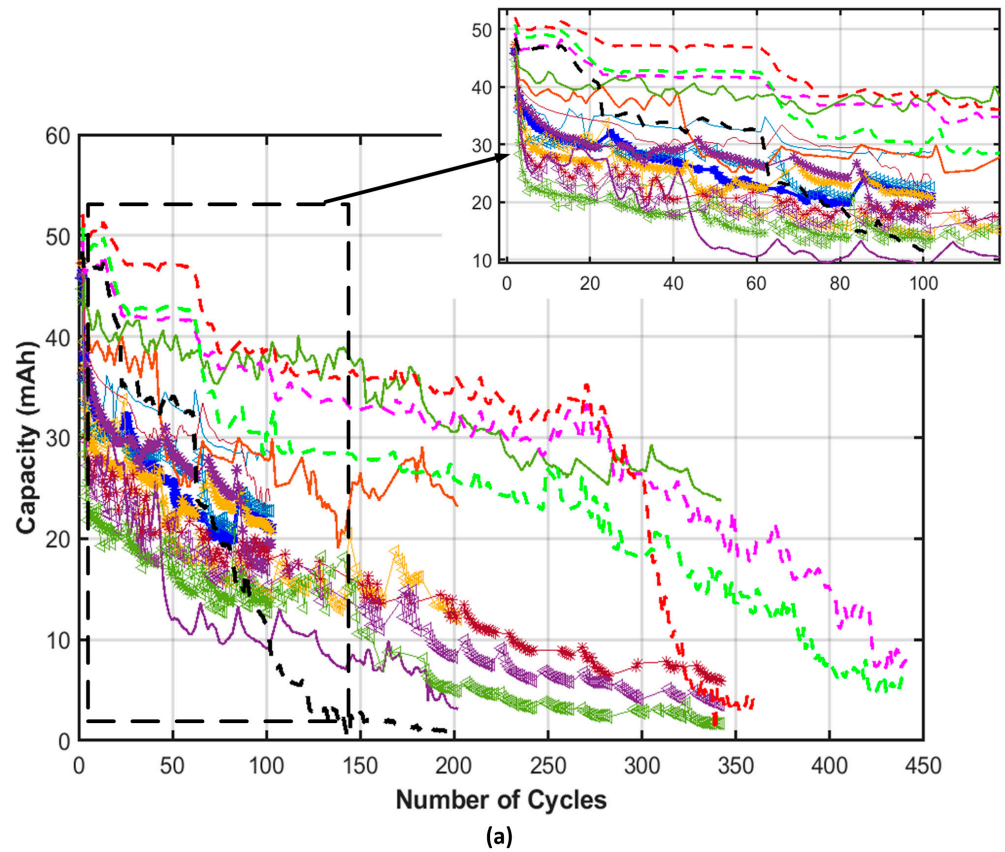

Figure 4. Capacity of sample cells over cycling. (**a**) Capacity of all samples with first 100 cycles highlighted. (**b**) Capacities of Batch A showing cycles of high discharge current.
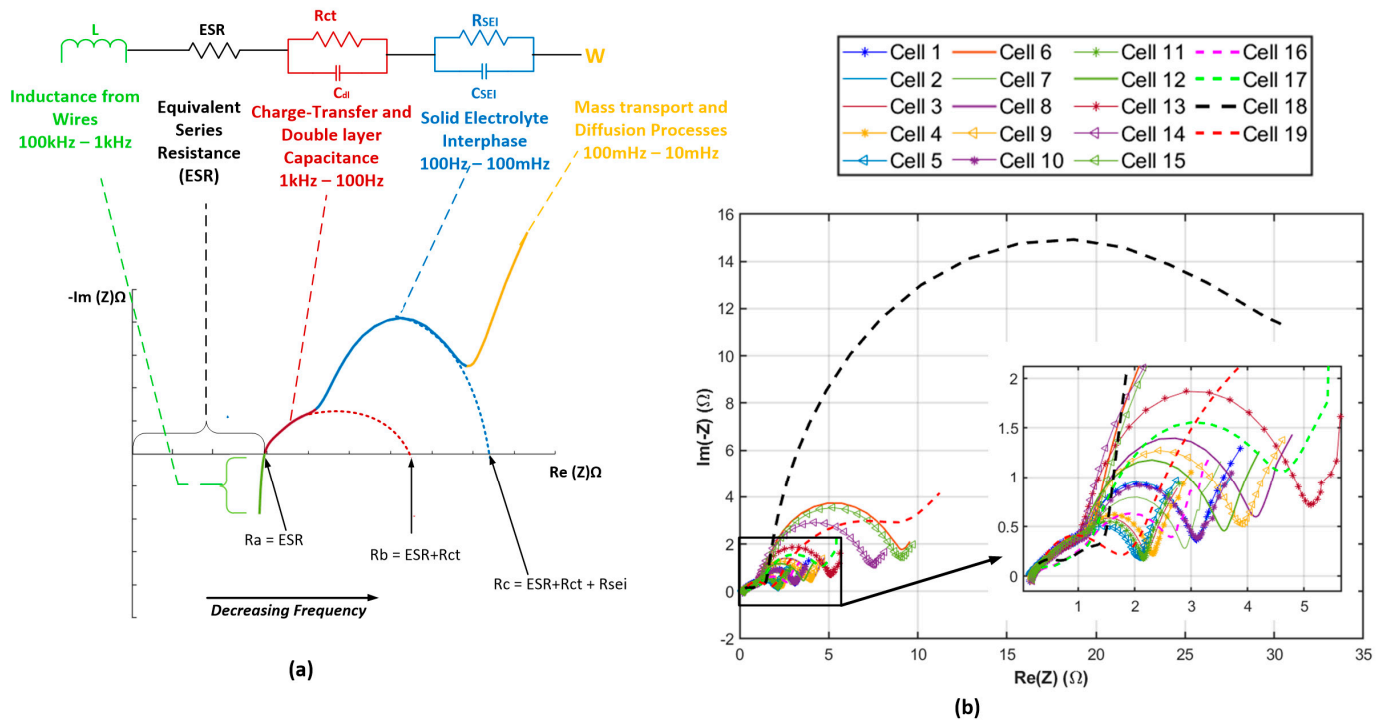
Figure 5. Sample cells EIS impedance response. (**a**) Generic EIS response of commercial batteries. (**b**) EIS response of cells in their aged state.
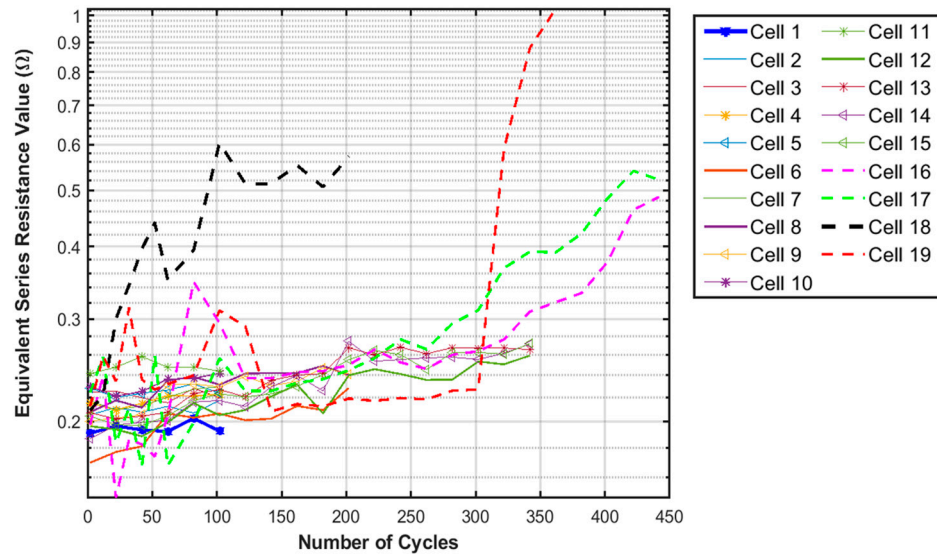

Figure 6. Equivalent series resistance of sample cells extracted from EIS impedance response.

Overall, the samples were aged between 102 and 442 cycles, with two cells having capacities above 60%, eight cells with capacities between 60% and 30%, and nine cells with capacities below 30%. The ESR ranged from 0.22 to 1.02 Ω. Between different cells, an average 0.13 Ω change in ESR was observed for cells in Batch A and 4 mΩ for cells in Batch B. Based on the responses of resistors in RoC, although these values can be detected, the accuracy would be low. In automative applications, cells whose capacity has fallen below 70% at a given state of charge are considered aged [26]. However, no generalised ESR threshold has been established in the literature that universally indicates a battery problem, although different values and descriptions, such as a 20–30% increment; slight changes; and double initial values have been suggested [27–30]. ESR increases with age and varies based on battery type and operating conditions. A significant rise in ESR compared to a

healthy cell of the same type and age, especially when combined with other health indicator changes, suggests potential battery degradation. Therefore, for this study, ESR together with capacity have been used to assess the aging of the sample cells and a reference for comparing the FDR-based impedance. The EIS impedance details of the cells in their new and aged states are summarised in Table 1.

3.2. Frequency Domain Reflectometry Responses

First, the resonance-based method was used in the cell responses before de-embedding. Based on the RLC responses, this method was projected to have both low sensitivity and accuracy within the resistive and capacitive ranges of the cell; hence, further analysis was not carried out. However, despite three outlier cells, the resonance frequency appears to be relatively constant, as well as the amplitude variation, as shown in Figure 7. This behaviour was also observed in the resonance response of the resistors, suggesting that relative changes in the resistive properties between different cells were detected. However, unlike the resistors, the changes in amplitude did not correlate with the ESR or capacities of the cells, as illustrated in Figure 7a and Figure 7b, respectively. This is an artefact of the limited accuracy and sensitivity of the setup within the range of values. In Masrakin et al. [9] and Skierucha [10], the probe used had direct contact with the material under test and had defined characteristics that were used to create and decouple the resonance circuit. However, in the case of a PCB with a cell, there is a hindrance in ensuring direct contact with the battery without its outer casing.
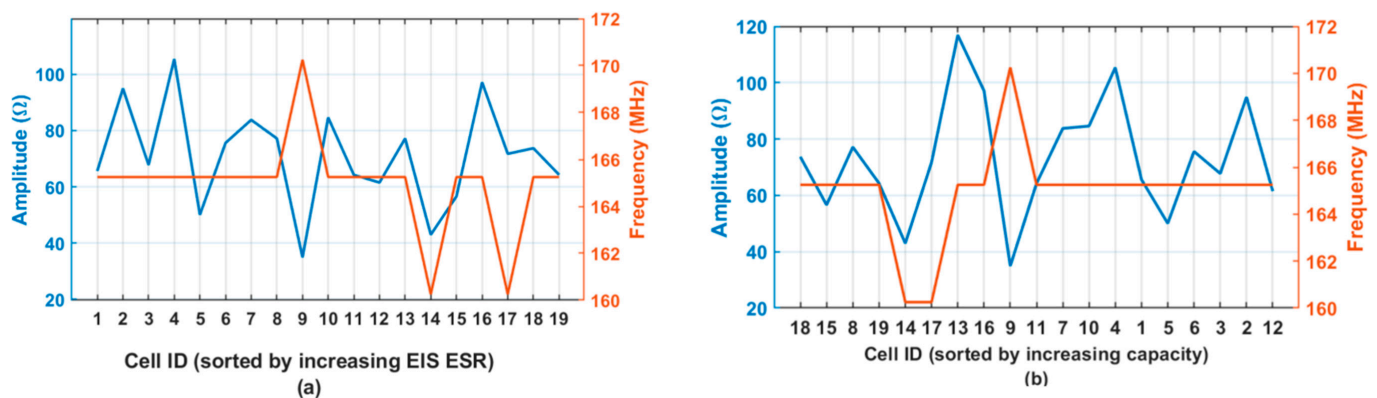

Figure 7. Resonance frequency and amplitude of sample cells from FDR responses. (**a**) FDR resonance amplitude and frequency over increasing cell ESR. (**b**) FDR resonance amplitude and frequency over increasing cell capacity.

In addition, defining cell dimensions when measured in the PCB at high frequencies becomes complicated, contributing to the inadequacy of the resonance-based method in accurately monitoring SoH changes.

Within the RoC, as shown in Figure 8, the post-compensation responses were relatively constant compared with the pre-compensation responses. In the pre-compensation responses, no consistent trend between the real part of the impedance and the ESR or capacity was observed, which is attributed to the limited accuracy and sensitivity in detecting low ohmic values. However, the reactive part of the impedance shows variations that are related to the increasing ESR values of the samples, as shown in Figure 8a. This trend was more significant in the pre-compensation responses, as shown in Figure 8a, than in the post-compensation stage. This echoes the pattern seen in the test on basic RLC elements, where accuracy is reduced after de-embedding; however, in the case of a cell, the complexity of the cell system is introduced. With respect to capacity, the pre-de-embedding responses of cells of Batch A (16–19) with less than 10% capacity were seen to have higher FDR reactance values than cells of Batch B within the RoC. Aside from this, no identifiable trend is seen between FDR reactance and cell capacity fade, which suggests that FDR reactance might be

influenced by degradation mechanisms that directly affect cell internal impedance more than capacity fade; hence, additional information other than capacity is required to relate FDR reactance to cell SoH.
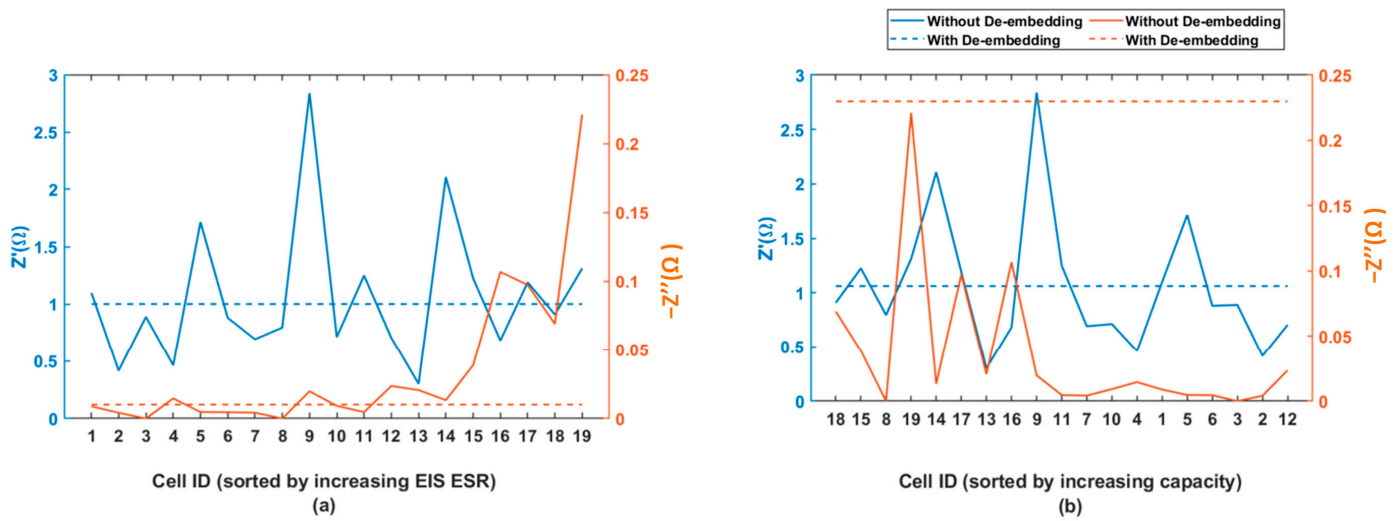

Figure 8. FDR Complex impedance of cells within RoC at 300 kHz. (**a**) FDR impedance over cells with samples sorted by increasing ESR. (**b**) FDR impedance over cells with samples sorted by increasing capacity.

Furthermore, the relationship between FDR reactance and ESR can be explained by the dielectric capacitive behaviour. At high frequencies, the ions within the electrolyte struggle to respond rapidly to fast time-varying signals, leading to the accumulation of charges at the electrode–electrolyte interface, which significantly influences the capacitive behaviour observed in high-frequency impedance measurements. As the cells aged, the increase in salts from electrolyte decomposition and reaction by-products further impeded ionic migration. The relationship between capacitive reactance and ESR can be attributed to the fact that both parameters are influenced by similar factors at the electrode–electrolyte interface. The observed correlation between the reactive impedance and ESR was further explored by comparing the ESR and FDR values over the lifetime of cells 16 and 19 in Figure 9.

These cells were chosen because they had a greater number of cycles, over which an existing trend could be established. Figure 9a,c compares how the cell capacity and FDR reactance change over cycling for the pre-compensation responses, whereas Figure 9b,d shows the same for the post-compensation stages. In both stages, the FDR reactance is inversely related to the cell capacity over cycling. A clearer trend is observed over the lifetime of a cell than that observed over different cells. This can be attributed to the presence of fewer variables when a single cell is considered. Furthermore, at cycle 300 of cell 19, after exposure to a high discharge current resulted in a 28% reduction capacity, ESR increased from 0.22 to 1.02 Ω. At this point, the FDR reactance also increased from 0.069 to 0.221 Ω pre-compensation, and from 0.0063 to 0.018 Ω post-compensation. This shows that a change of 0.8 Ω is detected as a 0.15 Ω and 0.01 Ω change with pre- and post-compensation, suggesting a reduced sensitivity with de-embedding.

Despite the existence of a trend that relates the FDR reactance within the RoC to the EIS-based ESR and the consistent increase over cycling, the relatively small magnitude of values seen in FDR reactance, particularly post-compensation, raises concerns regarding the sensitivity of the method for practical applications. System noise may easily over-shadow such subtle changes and potentially hinder real-world applicability. The identified trends provide a promising foundation for further research and refinement of FDR-based techniques to enhance the accuracy and applicability of battery SoH monitoring.
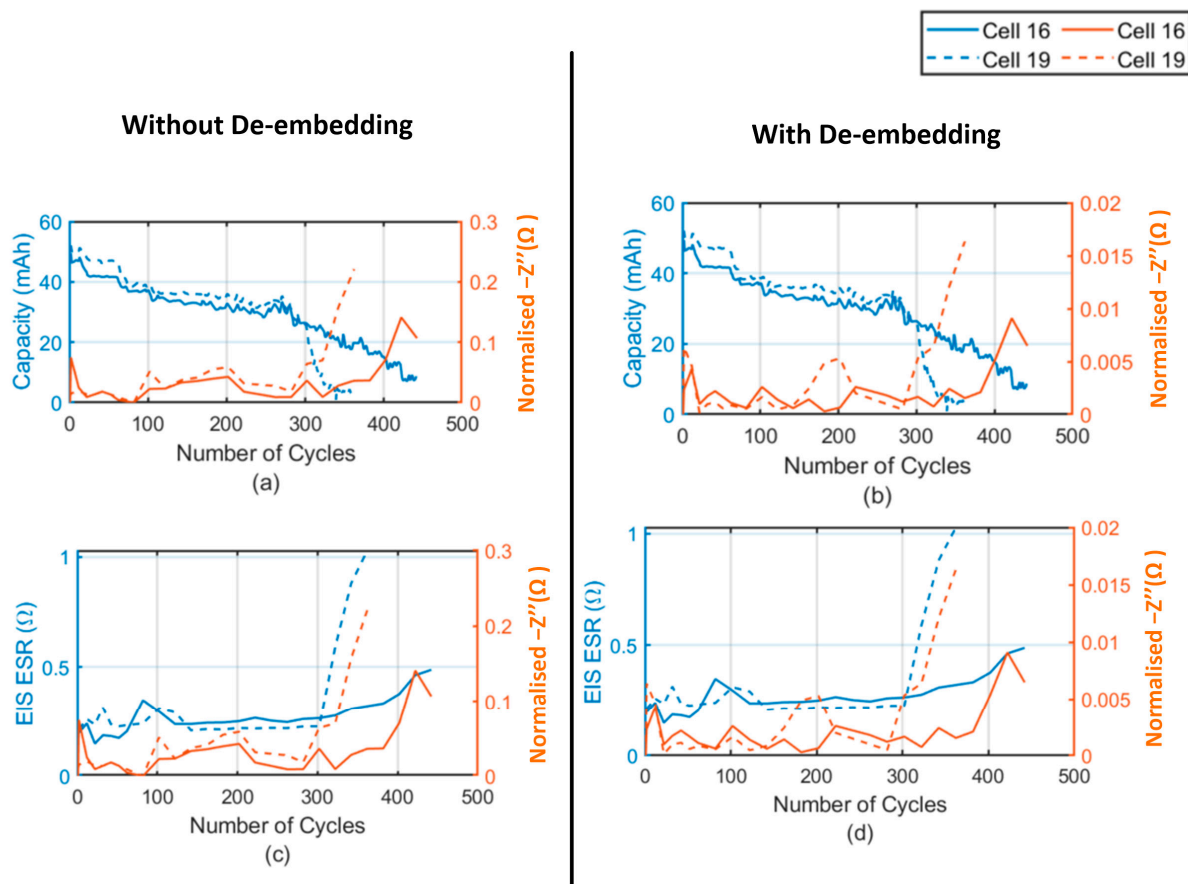
Figure 9. Relationship between normalised FDR reactance and health indicators over cycling. (**a**) Pre-compensation normalised FDR reactance and capacity fade over cycling. (**b**) Post-compensation normalised FDR reactance and capacity fade over cycling. (**c**) Pre-compensation normalised FDR reactance and EIS-measured ESR over cycling. (**d**) Post-compensation normalised FDR reactance and EIS ESR over cycling.

4. Conclusions

In conclusion, this study investigated the utilisation of FDR as a potential tool for monitoring the SoH of batteries. A measurement setup based on the ring resonator and the S_{21} method with a VNA was used to determine battery impedance. To ensure accuracy, system calibration and de-embedding procedures were employed to mitigate any interference from the test setup. Firstly, tests on different values of resistors, inductors, and capacitors revealed changes in these values, which were accurately detected between 300 kHz and 40 MHz with reduced accuracy within 5–10 mΩ, 0.1–1 nH, and 10–200 pF value ranges. Resistors, inductors, and capacitors resonated between 2 and 355 MHz. The resonance frequency of capacitors and inductors decreased with increasing values, while that of resistors remained relatively stable. However, both pre- and post-compensation responses exhibited limited sensitivity and accuracy, particularly with higher capacitance and inductance values. Nineteen LIR2032 commercial sample cells were used in the study. These were subjected to cyclic aging using the CC–CV cycling method. The results indicated a clear degradation in battery performance over cycles, evidenced by capacity loss and increased ESR. EIS analysis confirmed the effects of aging due to electrolyte decomposition and SEI layer growth. While the resonance method lacked sensitivity for cell capacitance, it effectively identified patterns of resistance change over the different sample cells. Despite promising correlations between FDR reactance and ESR trends, challenges remain in achieving consistent sensitivity and accuracy, particularly post-compensation. While FDR presents itself as a promising prospect for lithium-ion battery SoH monitoring,

further research is imperative to enhance its sensitivity and address practical limitations to reduce its susceptibility to system noise. By advancing FDR-based methodologies and integrating complementary approaches, such as improved de-embedding protocols and noise mitigation strategies, the potential for accurate and reliable battery health monitoring that incorporates dielectric permittivity detection could be realised.

Author Contributions: Conceptualisation, V.P., M.M. and C.T.; Formal analysis, A.B.A.-A., M.M. and C.T.; Funding acquisition, V.P.; Methodology, A.B.A.-A., V.P. and M.M.; Resources, V.P.; Supervision, V.P., M.M. and C.T.; Writing—original draft, A.B.A.-A.; Writing—review and editing, V.P. and C.T. All authors have read and agreed to the published version of the manuscript.

Data Availability Statement: The original contributions presented in this study are included in the article; further inquiries can be directed to the authors.

Conflicts of Interest: The authors declare no conflicts of interest.

References

1. Berecibar, M.; Gandiaga, I.; Villarreal, I.; Omar, N.; Van Mierlo, J.; Van den Bossche, P. Critical review of state of health estimation methods of Li-ion batteries for real applications. *Renew. Sustain. Energy Rev.* **2016**, *56*, 572–587. [CrossRef]
2. Meddings, N.; Heinrich, M.; Overney, F.; Lee, J.-S.; Ruiz, V.; Napolitano, E.; Seitz, S.; Hinds, G.; Raccichini, R.; Gaberšček, M.; et al. Application of electrochemical impedance spectroscopy to commercial Li-ion cells: A review. *J. Power Sources* **2020**, *480*, 228742. [CrossRef]
3. Birkl, C.R.; Roberts, M.R.; McTurk, E.; Bruce, P.G.; Howey, D.A. Degradation diagnostics for lithium ion cells. *J. Power Sources* **2017**, *341*, 373–386. [CrossRef]
4. Perry, D.; Mamlouk, M. Probing mass transport processes in Li-ion batteries using electrochemical impedance spectroscopy. *J. Power Sources* **2021**, *514*, 230577. [CrossRef]
5. Zhang, Y.; Tang, Q.; Zhang, Y.; Wang, J.; Stimming, U.; Lee, A.A. Identifying degradation patterns of lithium ion batteries from impedance spectroscopy using machine learning. *Nat. Commun.* **2020**, *11*, 1706. [CrossRef] [PubMed]
6. Furse, C.M.; Kafal, M.; Razzaghi, R.; Shin, Y.-J. Fault Diagnosis for Electrical Systems and Power Networks: A Review. *IEEE Sens. J.* **2021**, *21*, 888–906. [CrossRef]
7. Furse, C.; Chung, Y.; Lo, C.; Pendayala, P. A critical comparison of reflectometry methods for location of wiring faults. *Smart Struct. Syst.* **2006**, *2*, 25–46. [CrossRef]
8. Glass, S.W.; Fifield, L.S.; Jones, A.M.; Hartman, T.S. Frequency Domain Reflectometry Modeling and Measurement for Non-destructive Evaluation of Nuclear Power Plant Cables. In Proceedings of the 18th International Conference on Environmental Degradation of Materials in Nuclear Power Systems—Water Reactors, Portland, OR, USA, 13–17 August 2017; Jackson, J., Paraventi, D., Wright, M., Eds.; Springer International Publishing: Cham, Switzerland, 2019; pp. 1267–1280.
9. Masrakin, K.; Malek, S.A.; Ibrahim, S.Z.; Rahim, H.A.; Dewani, A.A. Dielectric Properties Characterization of Material Under Test using Microstrip Ring Resonator. *J. Phys. Conf. Ser.* **2021**, *1755*, 012017. [CrossRef]
10. Skierucha, W.; Wilczek, A. A FDR Sensor for Measuring Complex Soil Dielectric Permittivity in the 10–500 MHz Frequency Range. *Sensors* **2010**, *10*, 3314–3329. [CrossRef] [PubMed]
11. Landinger, T.F.; Schwarzberger, G.; Jossen, A. High frequency impedance characteristics of cylindrical lithium-ion cells: Physical-based modeling of cell state and cell design dependencies. *J. Power Sources* **2021**, *488*, 229463. [CrossRef]
12. Talie, A.P.; Pribyl, W.A.; Hofer, G. Electric Vehicle Battery Management System Using Power Line Communication Technique. In Proceedings of the 2018 14th Conference on Ph.D. Research in Microelectronics and Electronics (PRIME), Prague, Czech Republic, 2–5 July 2018; pp. 225–228. [CrossRef]
13. Bolsinger, C.; Brix, J.; Dragan, M.; Birke, K.P. Investigating and modeling the transmission channel of a prismatic lithium-ion cell and module for powerline communication. *J. Energy Storage* **2017**, *10*, 11–19. [CrossRef]
14. Reuter, M.; Friedl, T.; Tenbohlen, S.; Kohler, W. Emulation of conducted emissions of an automotive inverter for filter development in HV networks. In Proceedings of the IEEE International Symposium on Electromagnetic Compatibility, Denver, CO, USA, 5–9 August 2013; pp. 236–241. [CrossRef]
15. Keysight Technologies. Ultra-Low Impedance Measurements Using 2-Port Measurements. Application Note, EN5989-5935. 2014. Available online: http://literature.cdn.keysight.com/litweb/pdf/5989-5935EN.pdf (accessed on 20 April 2024).
16. Landinger, T.F.; Schwarzberger, G.; Jossen, A. A Novel Method for High Frequency Battery Impedance Measurements. In Proceedings of the 2019 IEEE International Symposium on Electromagnetic Compatibility, Signal & Power Integrity (EMC+SIPI), New Orleans, LA, USA, 22–26 July 2019; pp. 106–110. [CrossRef]

17. Hackl, H.; Ibel, M.; Landinger, T.F.; Pommerenke, D.J.; Auinger, B. Li-Ion Cell Impedance Measurement Using Open/Short/Load Compensation for De-Embedding. In Proceedings of the 2021 Joint IEEE International Symposium on Electromagnetic Compatibility Signal and Power Integrity, and EMC Europe, EMC/SI/PI/EMC Europe 2021, Virtual, 13 August 2021; pp. 190–195. [CrossRef]
18. Landinger, T.F.; Schwarzberger, G.; Jossen, A. A Physical-Based High-Frequency Model of Cylindrical Lithium-Ion Batteries for Time Domain Simulation. *IEEE Trans. Electromagn. Compat.* **2020**, *62*, 1524–1533. [CrossRef]
19. Roy, S.; Khan, F. Detection of Degraded/Aged Cell in a Li-ion Battery Pack using Spread Spectrum Time Domain Reflectometry (SSTDR). In Proceedings of the 2020 IEEE Applied Power Electronics Conference and Exposition (APEC), New Orleans, LA, USA, 15–19 May 2020; pp. 1483–1488. [CrossRef]
20. NEXCell Battery Company. Material Safety Data Sheet Index-25 Material Safety Data Sheet. 2021. Available online: https://owlpowersolutions.com/wp-content/uploads/2022/08/LIR2032-MSDS.pdf (accessed on 17 April 2021).
21. Woehrle, T. Lithium-ion cell. In *Lithium-Ion Batteries: Basics and Applications*; Korthauer, R., Ed.; Springer: Berlin/Heidelberg, Germany, 2018; pp. 101–111. [CrossRef]
22. RS Components Ltd. RS Pro Lithium-Ion Button Battery Datasheet. 2022. Available online: https://docs.rs-online.com/b16a/0900766b8170b05c.pdf (accessed on 16 February 2021).
23. Pico Technology Ltd. PicoVNA 6 and 8.5 GHz Vector Network Analyzers User Manual. 2020. Available online: https://www.picotech.com/download/manuals/picovna-vector-network-analyzer-users-guide.pdf (accessed on 16 February 2021).
24. Keysight Technologies Ltd. Performing Impedance Analysis with the E5061B ENA Vector Network Analyzer. Application Note, 5991-0213EN. 2018. Available online: https://www.keysight.com/gb/en/assets/7018-03423/application-notes/5991-0213.pdf (accessed on 12 March 2022).
25. Sun, B.; Bian, J.; Ruan, H.; Zhang, W.; Ren, P.; Cong, X. Modeling Study for Li-ion Batteries Considering High-frequency Inductance Characteristics Based on Electrochemical Impedance Spectroscopy. *DEStech Trans. Environ. Energy Earth Sci.* **2019**, CEEE2018-32. [CrossRef] [PubMed]
26. Marin-Montin, J.; Zurita-Gotor, M.; Montero-Chacón, F. Numerical Analysis of Degradation and Capacity Loss in Graphite Active Particles of Li-Ion Battery Anodes. *Materials* **2022**, *15*, 3979. [CrossRef] [PubMed]
27. Dechent, P.; Barbers, E.; Epp, A.; Jöst, D.; Li, W.; Sauer, D.U.; Lehner, S. Correlation of Health Indicators on Lithium-Ion Batteries. *Energy Technol.* **2023**, *11*, 2201398. [CrossRef]
28. Yao, Y.; Li, H.; Zhou, Z.; Cai, Z.; Li, Z. Prediction of lithium-ion battery capacity and remaining useful life based on characteristic ohmic resistance model. In Proceedings of the 2022 Chinese Automation Congress, CAC, Xiamen, China, 25–27 November 2022; pp. 5569–5574. [CrossRef]
29. Zhao, C.; Yin, H.; Ma, C. Equivalent Series Resistance-based Real-time Control of Battery-Ultracapacitor Hybrid Energy Storage Systems. *IEEE Trans. Ind. Electron.* **2020**, *67*, 1999–2008. [CrossRef]
30. Zaman, M.H.M.; Mustafa, M.M.; Hussain, A. Critical equivalent series resistance estimation for voltage regulator stability using hybrid system identification and neural network. *Int. J. Adv. Sci. Eng. Inf. Technol.* **2017**, *7*, 1381. [CrossRef]